

## Supplementary Information File

### Trap Engineering Through Chemical Doping for Ultralong X-ray Persistent Luminescence and Anti-Thermal Quenching in $\text{Zn}_2\text{GeO}_4$

Annu Balhara<sup>1,2</sup>, Santosh K. Gupta<sup>1,2\*</sup>, Malini Abraham<sup>3,4</sup>, Brindaban Modak,<sup>2,5</sup> Subrata Das<sup>3,4</sup>, Chandrani Nayak<sup>6</sup>, Harshini V. Annadata<sup>7</sup>, Mohit Tyagi<sup>2,8</sup>

<sup>1</sup>Radiochemistry Division, Bhabha Atomic Research Centre, Trombay, Mumbai-400085, India

<sup>2</sup>Homi Bhabha National Institute, Anushaktinagar, Mumbai – 400094, India

<sup>3</sup>Materials Science and Technology Division, CSIR-National Institute for Interdisciplinary Science and Technology, Thiruvananthapuram, Kerala 695019

<sup>4</sup>Academy of Scientific and Innovative Research (AcSIR), Ghaziabad-201002, India

<sup>5</sup>Chemistry Division, Bhabha Atomic Research Centre, Trombay, Mumbai-400085, India

<sup>6</sup>Atomic and Molecular Physics Division, Bhabha Atomic Research Centre, Mumbai-400085.

<sup>7</sup>Beamline Development & Application Section, Bhabha Atomic Research Centre, Mumbai 400085

<sup>8</sup>Technical Physics Division, Bhabha Atomic Research Centre, Trombay, Mumbai-400085, India

\*To whom correspondence should be addressed. Electronic mail: \*santoshg@barc.gov.in/  
santufnd@gmail.com (SKG)

#### S1. Synthesis

$\text{Zn}_2\text{GeO}_4$  and  $\text{Zn}_2\text{GeO}_4:\text{Pr}^{3+}$  ( $x = 0.005, 0.01, 0.02,$  and  $0.05$ ) samples were synthesized *via* a two-step high temperature solid-state route. The precursors of ZnO (99.99%),  $\text{GeO}_2$  (99.99%),  $\text{Pr}_6\text{O}_{11}$  (99.99%) were mixed in stoichiometric amounts and ground finely. The powder obtained were sintered at 900 °C for 15 h, at a heating rate of 10 °C/min in air atmosphere. Then, all the samples were annealed at 1200 °C for 15 h after an intermediate grinding for 15 min.

#### S2. Instrumentation

The powder XRD patterns were acquired on a Proto-AXRD bench top system in the  $2\theta$  range of 15-80° and a scan rate of 1°/min. Small-Angle X-ray Diffraction (SAXD) patterns were recorded on a XEUSS SAXS/WAXS system from Xenocs operated at 0.60 mA and 50 kV in

the transmission mode. Rietveld refinement was performed using FullProf software. The refined crystal structure was obtained with the help of Vesta software. Fourier Transform Infrared Spectroscopy (FTIR) was performed with a diamond ATR mode on a Bruker Alpha FTIR spectrometer in the scanning range from 400 to 4000  $\text{cm}^{-1}$ . Raman spectral measurements were carried out on a Seki's STR300 Raman spectrometer at a 532 nm excitation wavelength. X-ray photoelectron spectroscopy (XPS) was carried out on PHI 5000 Versa Prob II, FEI Inc. X-ray Absorption Spectroscopy (XAS) measurements of Pr doped  $\text{Zn}_2\text{GeO}_4$  samples have been carried out at Zn K edge (9659 eV) and Ge K-edge (11103 eV) in Transmission mode and Pr  $L_3$  edge (5964 eV) in fluorescence mode at the Scanning EXAFS Beamline (BL-9) at the Indus-2 Synchrotron Source (2.5 GeV, 200 mA) at the Raja Ramanna Centre for Advanced Technology (RRCAT), Indore, India.<sup>1, 2</sup> The energy dispersive spectroscopy (EDS) and elemental mapping were performed using Bruker Nano GmbHX Flash detector 410-M (Berlin, Germany). The PL and PLE spectra were recorded with a continuous Xenon lamp (450 W) source on a FLS-1000 fluorescence spectrometer (Edinburgh Instruments, U.K.), and visible-PMT as the detector. Emission photographs were captured under 254 and 365 nm UV lamp by Nikon camera. Low temperature dependence PL studies were performed using cryostat assembly with FLS-1000 fluorescence spectrometer and liquid nitrogen as coolant. Temperature-dependent PL emission spectra above RT were recorded on a Yvon Fluorolog 3 spectrofluorimeter with a 450 W Xenon Flash lamp as the exciting source (outsourced). The electroluminescence properties were measured using a high sensitivity spectrophotometer Maya 2000 Pro with a 280 nm UV LED as a source. Quantum yield measurements were carried out using integrated sphere. Thermoluminescence measurements were carried out on Riso TL/OSL-DA-15 reader system equipped with a 7.5 mm Hoya U-340 detection filter. Low-temperature electron paramagnetic resonance (EPR) studies at 100 K were performed on a Bruker EMX Series spectrometer using X band frequency (9.5 GHz) and 100 kHz field modulation. The persistent luminescence decay time was measured using Hamamatsu PMT R374 coupled with photon counting unit C8855-01, and power supply c9727. The Cu X-ray tube was operated at 40kV and 30 mA to irradiate the sample for 60 seconds and then the decay of intensity with time was measured after switching off the X-rays. For recording the image after X-ray irradiation, a homemade black box having monochrome CCD was used. The sample was mounted on a disk facing 100 kV and 5 mA X-rays and the glow was recorded after switching off the X-rays. The electrochemical impedance spectroscopic (EIS) measurements were performed using an electrochemical work

station (CHI 760E, USA) in a frequency range of 100 mHz to 100 kHz in an open circuit condition.

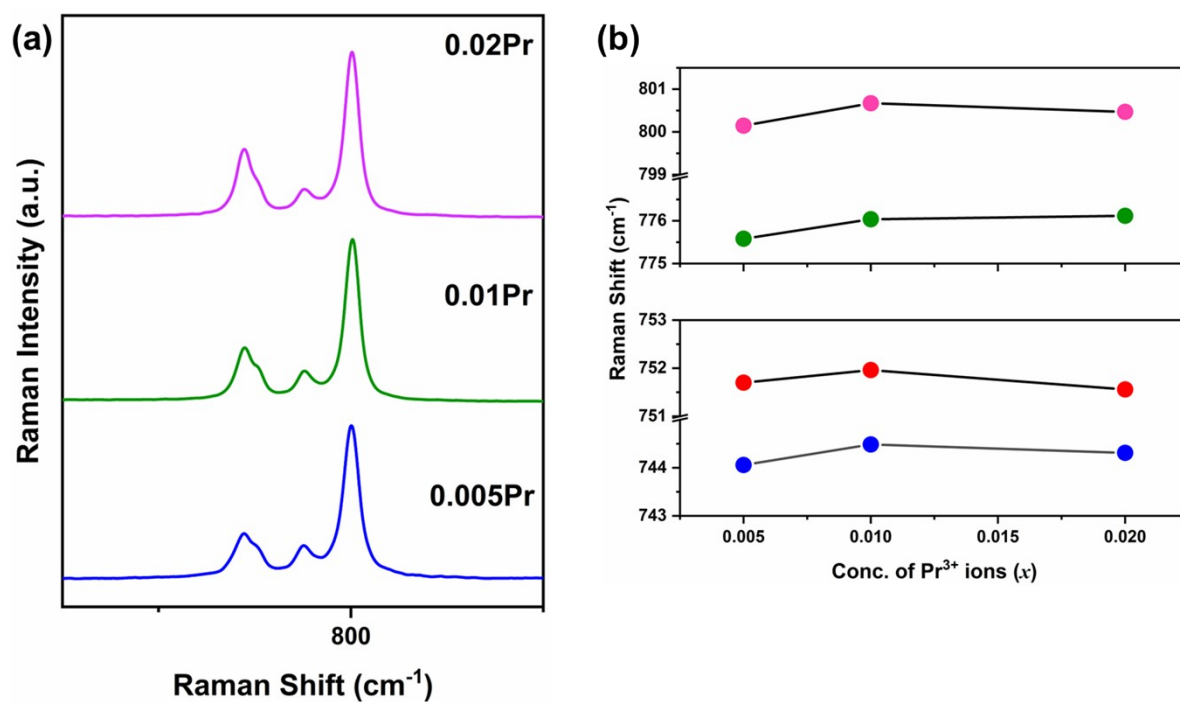


Figure S1: (a) Raman spectra  $\text{Zn}_2\text{GeO}_4:\text{Pr}^{3+}$  ( $x = 0.005, 0.01, 0.02$ ) samples, (b) Shift in Raman peaks as a function of  $\text{Pr}^{3+}$  concentration ( $x$ ).

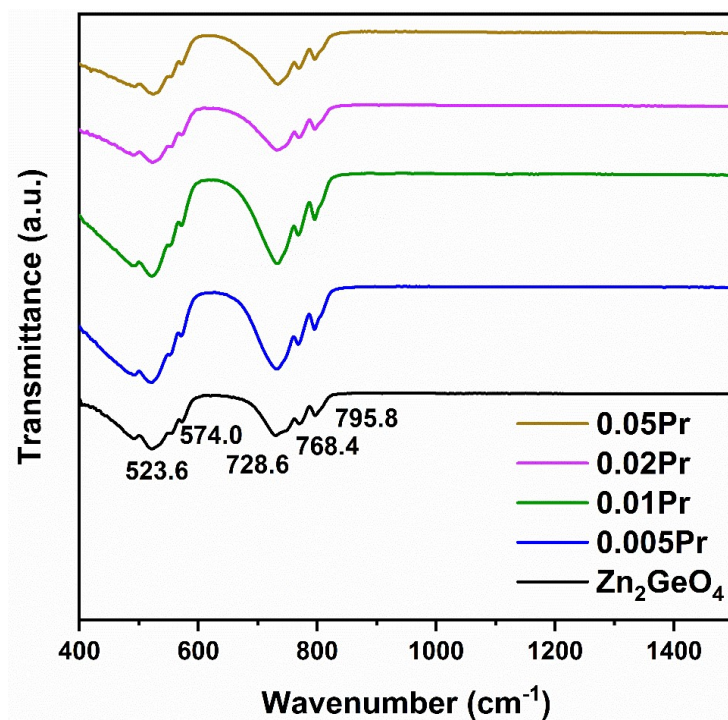


Figure S2: FTIR spectra of  $\text{Zn}_2\text{GeO}_4:\text{Pr}^{3+}$  ( $x = 0, 0.005, 0.01, 0.02$  and  $0.05$ ) samples.

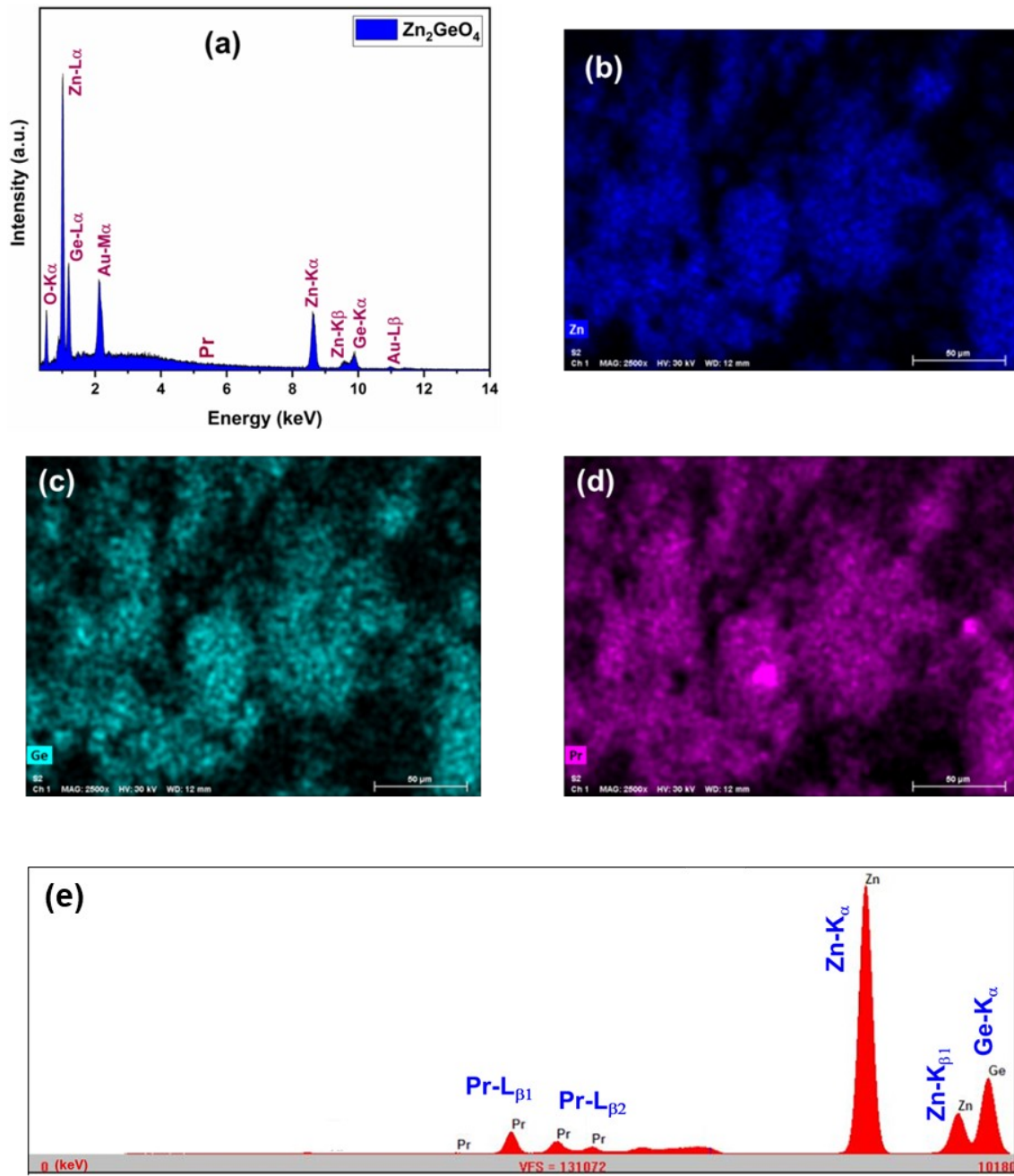


Figure S3: (a) EDS spectra of 0.01Pr sample, and elemental mapping for (b) Zn, (c) Ge, and (d) Pr, and (e) ED-XRF spectra for Zn<sub>2</sub>GeO<sub>4</sub>:0.05Pr sample.

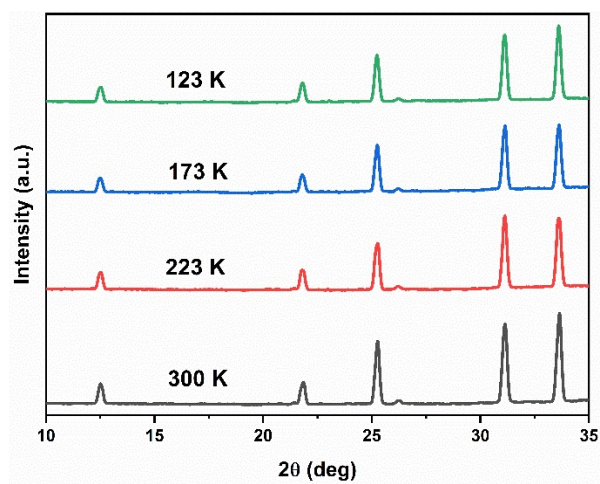


Figure S4: SAXD patterns of  $Zn_2GeO_4$  recorded at different temperatures below 300 K.

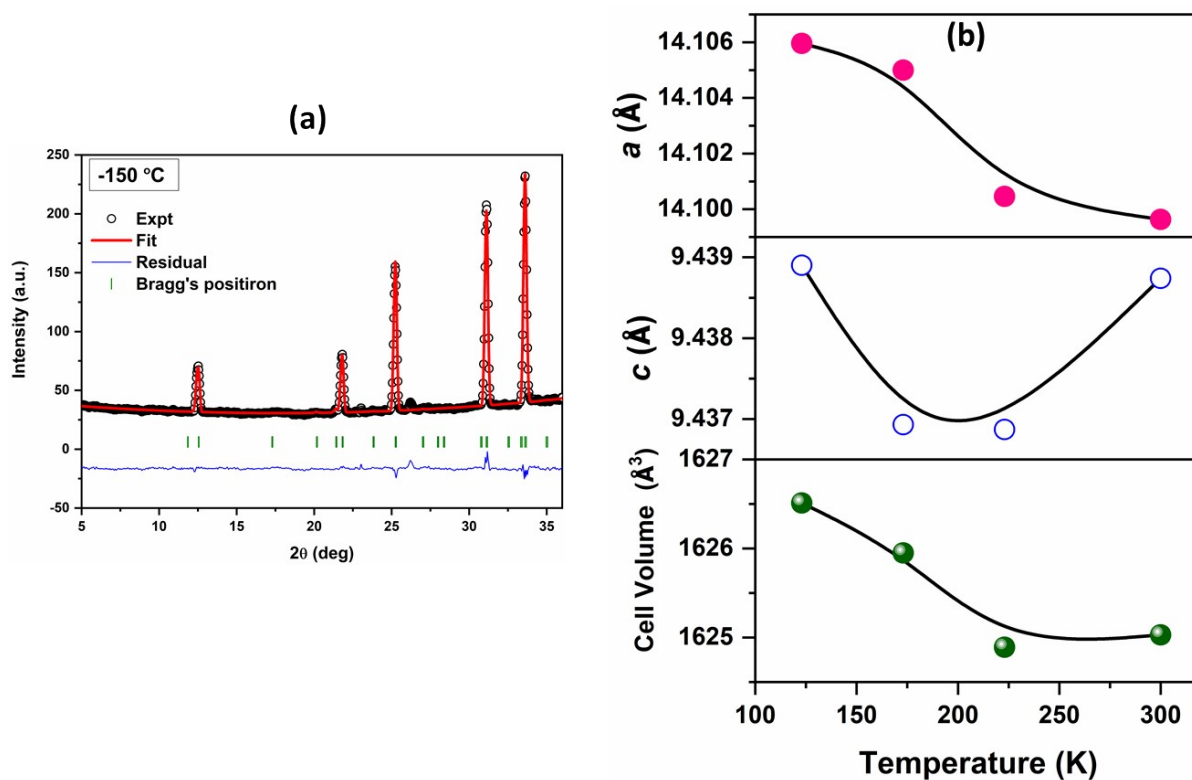


Figure S5: (a) Rietveld refinement of XRD data of  $Zn_2GeO_4$  recorded at 123 K, (b) Variation in the lattice constants with temperature.

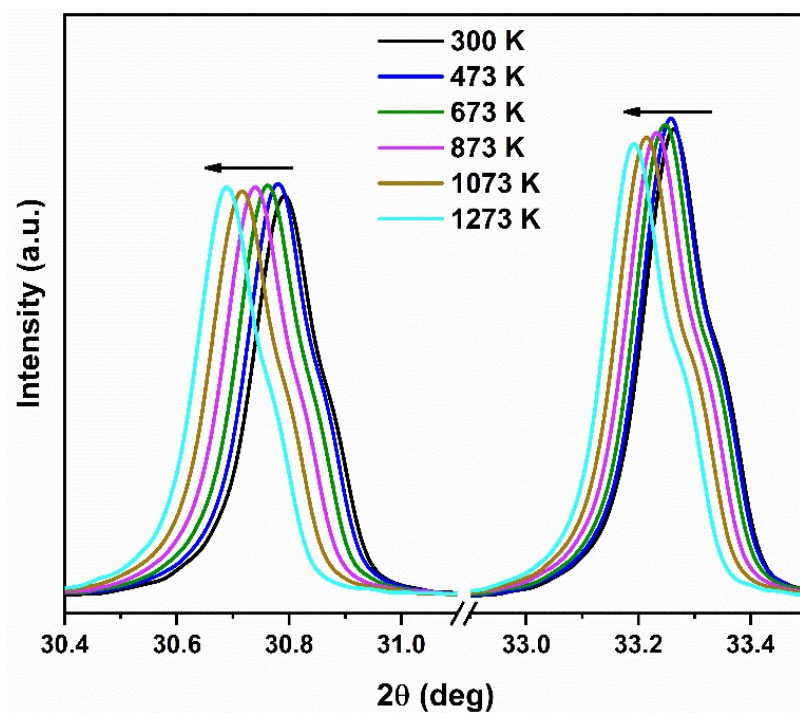
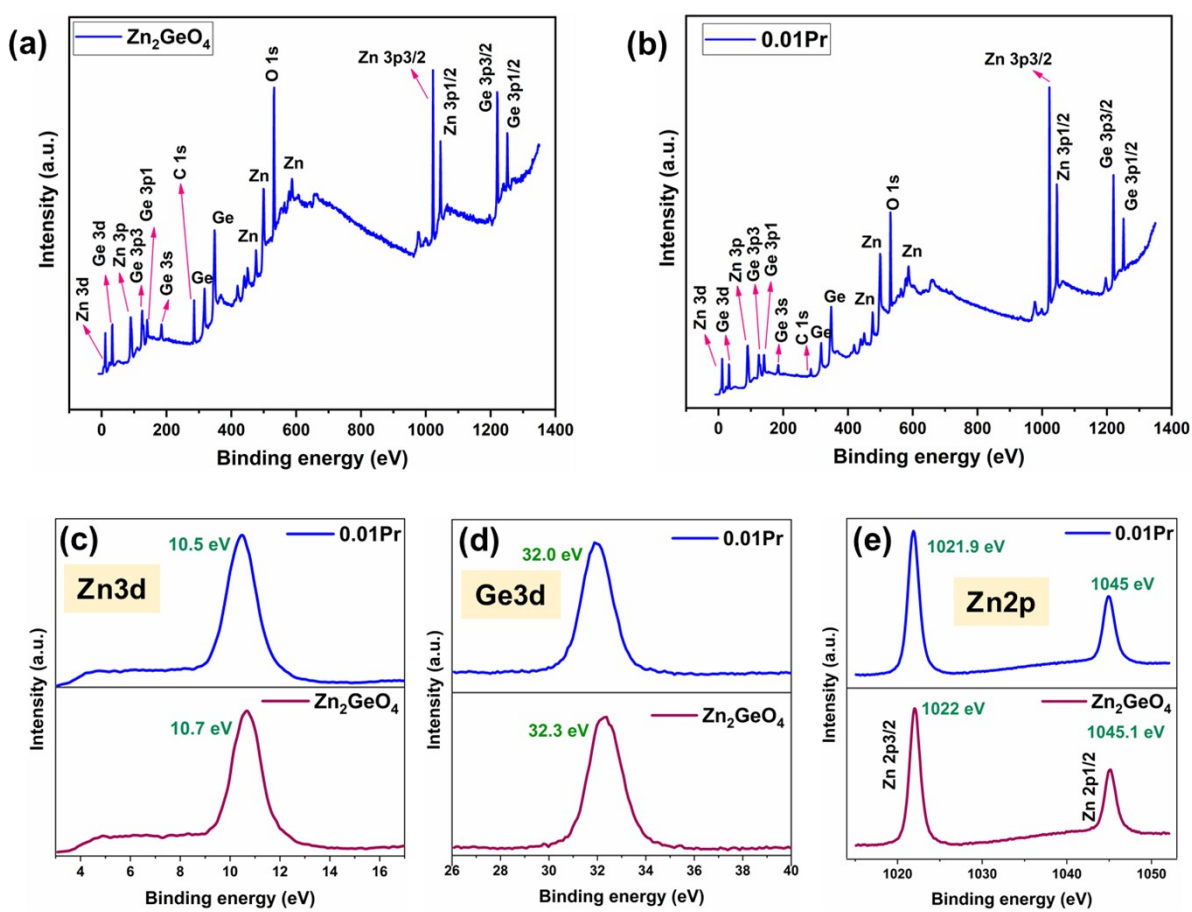
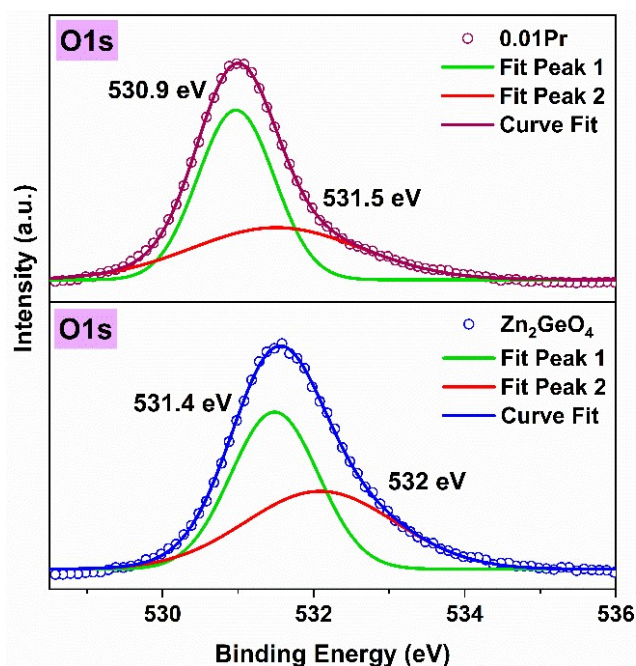


Figure S6: XRD patterns of  $\text{Zn}_2\text{GeO}_4$  recorded at different temperatures above 300 K representing the thermal expansion of  $\text{Zn}_2\text{GeO}_4$  lattice.



**Figure S7: XPS survey spectrum of (a)  $\text{Zn}_2\text{GeO}_4$  and (b) 0.01Pr samples, and XPS spectra of (c) Zn3d, (d) Ge3d, and (e) Zn3d for  $\text{Zn}_2\text{GeO}_4$  and 0.01Pr samples.**

# No significant shift in the binding energies of  $\text{Zn}2p_{3/2}$  and  $\text{Zn}2p_{1/2}$  peaks of undoped and Pr doped  $\text{Zn}_2\text{GeO}_4$  were observed and this can be ascribed to weak sensitivity of the Zn2p toward the local environment.



**Figure S8: Gaussian deconvoluted XPS spectra of O1s for  $\text{Zn}_2\text{GeO}_4$  and 0.01Pr samples.**

### S3. EXAFS Discussion

The beamline (Beamline, Indus-2 Synchrotron Source) uses a double crystal monochromator (DCM) which works in the photon energy range of 4-25 KeV with a resolution of  $10^4$  at 10 KeV. A 1.5 m horizontal pre-mirror with meridional cylindrical curvature is used prior to the DCM for collimation of the beam and higher harmonic rejection. The second crystal of the DCM is a saggital cylinder with radius of curvature in the range of 1.28-12.91 meters which provides horizontal focusing to the beam while another Rh/Pt coated bendable post mirror facing down is used for vertical focusing of the beam at the sample position. For the transmission mode measurement, three ionization chambers (300 mm length each) have been used for data collection, one ionization chamber for measuring incident flux ( $I_0$ ), second one for measuring transmitted flux ( $I_t$ ) and the third ionization chamber for measuring XAS spectrum of a reference metal foil for energy calibration. Appropriate gas pressure and gas mixtures have been chosen to achieve 10-20% absorption in first ionization chamber and 70-

90% absorption in second ionization chamber to improve the signal to noise ratio. The absorption coefficient  $\mu$  is obtained using the relation:

$$I_r = I_0 e^{-\mu x} \quad (1)$$

where,  $x$  is the thickness of the absorber. For measurements in the fluorescence mode, the sample is placed at  $45^\circ$  to the incident X-ray beam and the fluorescence signal ( $I_f$ ) is detected using a Si drift detector placed at  $90^\circ$  to the incident X-ray beam. An ionization chamber detector is used prior to the sample to measure the incident X-ray flux ( $I_0$ ) and the absorbance of the sample ( $\mu = \frac{I_f}{I_0}$ ) is obtained as a function of energy by scanning the monochromator over the specified energy range.

The EXAFS spectra have been extracted using the standard procedure.<sup>3-5</sup> In order to take care of the EXAFS oscillations in the absorption spectra, the energy dependent absorption coefficient  $\mu(E)$  has been converted to absorption function  $\chi(E)$  defined as follows:

$$\chi(E) = \frac{\mu(E) - \mu_0(E)}{\Delta\mu_0(E_0)} \quad (2)$$

where  $E_0$  absorption edge energy,  $\mu_0(E_0)$  is the bare atom background and  $\Delta\mu_0(E_0)$  is the step in the  $\mu(E)$  value at the absorption edge. After converting the energy scale to the photoelectron wave number scale ( $k$ ) as defined by,

$$k = \sqrt{\frac{2m(E - E_0)}{h^2}} \quad (3)$$

the energy dependent absorption coefficient  $\chi(E)$  has been converted to the wave number dependent absorption coefficient  $\chi(k)$ , where  $m$  is the electron mass. Finally,  $\chi(k)$  is weighted by  $k^2$  to amplify the oscillation at high  $k$  and the functions  $\chi(k)k^2$  are Fourier transformed in  $R$  space to generate the  $\chi(R)$  versus  $R$  plots (or FT-EXAFS spectra) in terms of the real distances from the centre of the absorbing atom. The  $k$  range used for Fourier transform is 2-11  $\text{\AA}^{-1}$  for Zn and Ge K edge data and 2-8  $\text{\AA}^{-1}$  for Pr  $L_3$  edge data. It should be mentioned here that a set of EXAFS data analysis program available within the Demeter software package<sup>6</sup> have been used for reduction and fitting of the experimental EXAFS data. This includes data reduction and Fourier transform to derive the  $\chi(R)$  versus  $R$  plots from the absorption spectra, generation of the theoretical EXAFS spectra starting from an assumed crystallographic structure and finally fitting of the experimental  $\chi(R)$  versus  $R$  data with the theoretical ones using the FEFF 6.0 code.

The goodness of fit has been determined by the value of the  $R_{factor}$  defined by:

$$R_{factor} = \sum \frac{[\text{Im}(\chi_{dat}(R_i) - \chi_{th}(R_i))]^2 + [\text{Re}(\chi_{dat}(R_i) - \chi_{th}(R_i))]^2}{[\text{Im}(\chi_{dat}(R_i))]^2 + [\text{Re}(\chi_{dat}(R_i))]^2} \quad (4)$$

Where,  $\chi_{dat}$  and  $\chi_{th}$  refer to the experimental and theoretical  $\chi(R)$  values respectively and Im and Re refer to the imaginary and real parts of the respective quantities.

**Table S1: Zn K edge EXAFS Fitting Results**

	<b>Zn<sub>2</sub>GeO<sub>4</sub></b>			<b>2% Pr doped Zn<sub>2</sub>GeO<sub>4</sub></b>			<b>5% Pr doped Zn<sub>2</sub>GeO<sub>4</sub></b>		
	$R_{factor} = 0.005$			$R_{factor} = 0.005$			$R_{factor} = 0.005$		
	<b>R (Å)</b>	<b>N</b>	<b><math>\sigma^2</math> (Å<sup>2</sup>)</b>	<b>R (Å)</b>	<b>N</b>	<b><math>\sigma^2</math> (Å<sup>2</sup>)</b>	<b>R (Å)</b>	<b>N</b>	<b><math>\sigma^2</math> (Å<sup>2</sup>)</b>
<b>Zn-O</b>	1.94 ±0.01	3.9 ±0.1	0.0066 ±0.0009	1.95 ±0.01	3.9 ±0.2	0.0067 ±0.0009	1.94 ±0.01	3.9 ±0.2	0.0069 ±0.0009
<b>Zn-Zn</b>	3.16 ±0.02	2.9 ±0.3	0.0011 ±0.0007	3.15 ±0.02	3.0 ±0.6	0.0010 ±0.0007	3.16 ±0.03	2.8 ±0.7	0.0010 ±0.0006
<b>Zn-Ge</b>	3.29 ±0.02	4.2 ±0.3	0.0010 ±0.0005	3.28 ±0.03	4.3 ±0.6	0.0010 ±0.0008	3.29 ±0.02	3.9 ±0.6	0.0010 ±0.0007

**Table S2: Ge K edge EXAFS Fitting Results**

	<b>Zn<sub>2</sub>GeO<sub>4</sub></b>			<b>2% Pr doped Zn<sub>2</sub>GeO<sub>4</sub></b>			<b>5% Pr doped Zn<sub>2</sub>GeO<sub>4</sub></b>		
	$R_{factor} = 0.007$			$R_{factor} = 0.005$			$R_{factor} = 0.006$		
	<b>R (Å)</b>	<b>N</b>	<b><math>\sigma^2</math> (Å<sup>2</sup>)</b>	<b>R (Å)</b>	<b>N</b>	<b><math>\sigma^2</math> (Å<sup>2</sup>)</b>	<b>R (Å)</b>	<b>N</b>	<b><math>\sigma^2</math> (Å<sup>2</sup>)</b>
<b>Ge-O</b>	1.75 ±0.01	4.2 ±0.1	0.0029 ±0.0004	1.76 ±0.01	4.2 ±0.1	0.0036 ±0.0005	1.76 ±0.01	4.2 ±0.1	0.0032 ±0.0005
<b>Ge-Zn</b>	3.27 ±0.02	8.4 ±0.6	0.0095 ±0.0007	3.28 ±0.01	8.6 ±0.6	0.0097 ±0.0008	3.27 ±0.01	8.4 ±0.6	0.0097 ±0.0006
<b>Ge-O</b>	3.52 ±0.05	5.8 ±0.5	0.0093 ±0.0033	3.52 ±0.03	5.5 ±0.5	0.0098 ±0.0028	3.51 ±0.03	5.5 ±0.5	0.0091 ±0.0027

**Table S3: Pr L<sub>3</sub> edge EXAFS Fitting Results**

	<b>2% Pr doped Zn<sub>2</sub>GeO<sub>4</sub></b>			<b>5% Pr doped Zn<sub>2</sub>GeO<sub>4</sub></b>		
	$R_{factor} = 0.011$			$R_{factor} = 0.011$		
	<b>R (Å)</b>	<b>N</b>	<b><math>\sigma^2</math> (Å<sup>2</sup>)</b>	<b>R (Å)</b>	<b>N</b>	<b><math>\sigma^2</math> (Å<sup>2</sup>)</b>
<b>Pr-O</b>	2.47±0.02	4.5±0.5	0.0076 ±0.0032	2.48±0.02	4.6±0.5	0.0081 ±0.0020

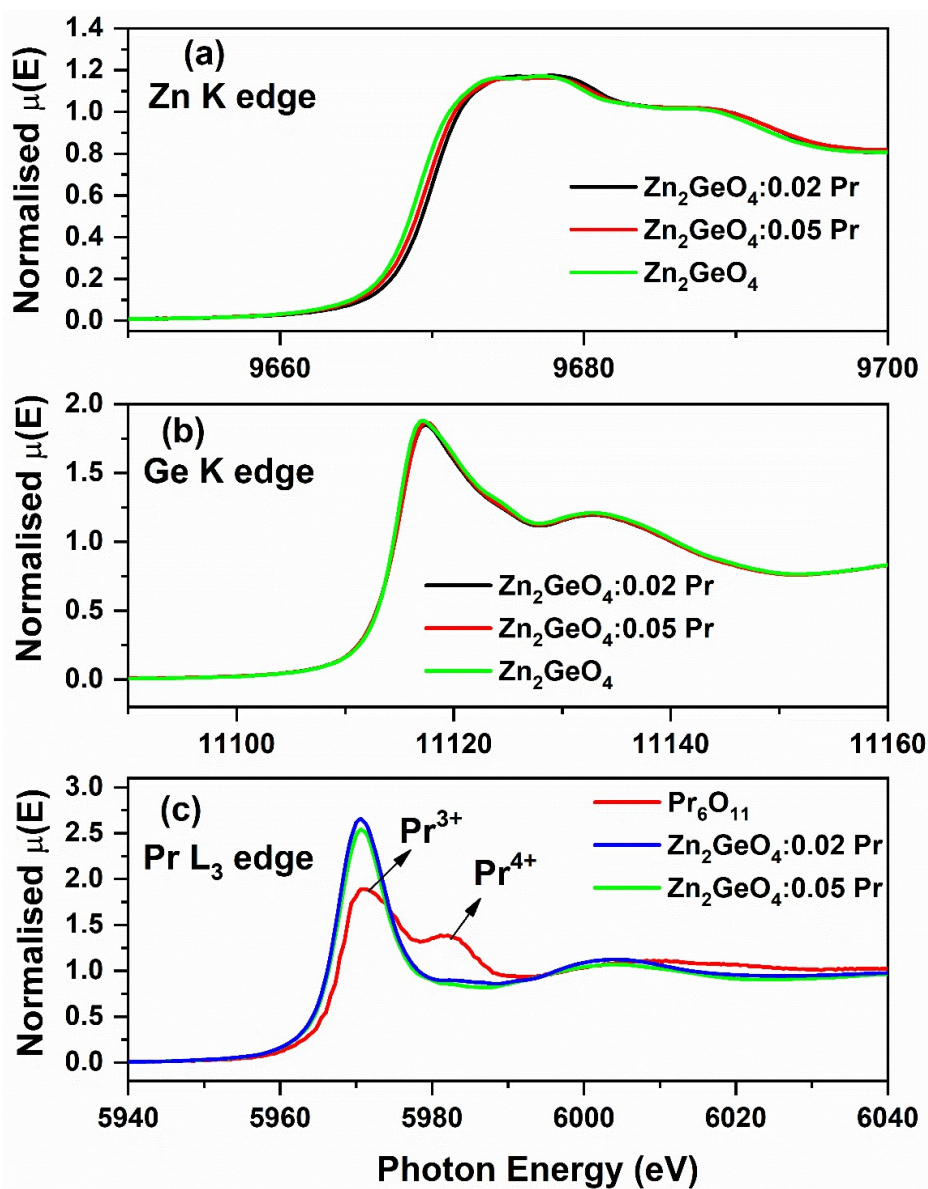
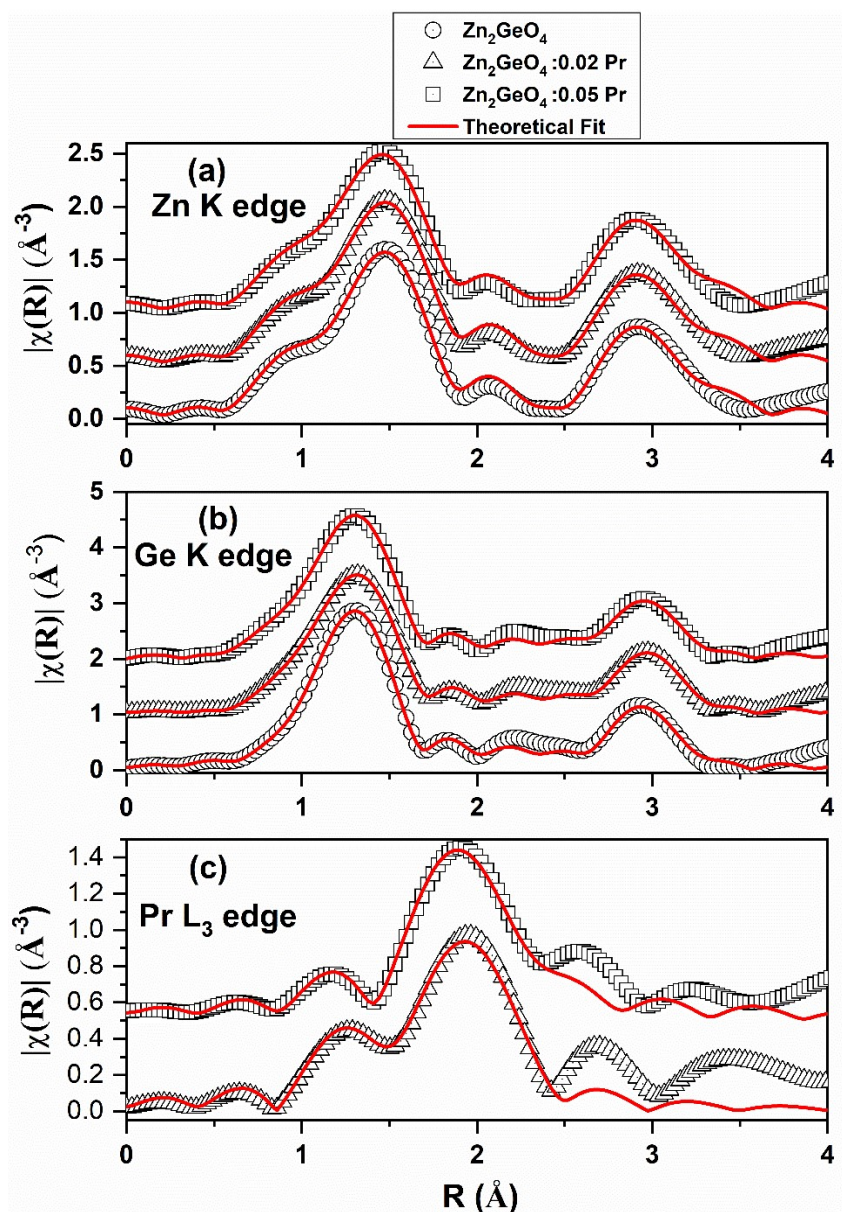


Figure S9: Normalized XANES spectra at (a) Zn K edge, (b) Ge K edge, and (c) Pr  $L_3$  edge (along with the  $\text{Pr}_6\text{O}_{11}$  standards) for undoped  $\text{Zn}_2\text{GeO}_4$ ,  $\text{Zn}_2\text{GeO}_4:0.02\text{Pr}$ , and  $\text{Zn}_2\text{GeO}_4:0.05\text{Pr}$ .



**Figure S10: Fourier-transformed EXAFS spectra and fitting of EXAFS spectrum for (a) Zn K edge, (b) Ge K edge, and (c) Pr  $L_3$  edge for undoped  $Zn_2GeO_4$ ,  $Zn_2GeO_4:0.02Pr$ , and  $Zn_2GeO_4:0.05Pr$ .**

## S4. DFT discussion

### *S4.1 Computational Methodology*

All the DFT calculations have been carried out using Vienna ab initio simulation package (VASP).<sup>7, 8</sup> Perdew–Burke–Ernzerhof (PBE) functional of the generalized gradient approximations (GGA) has been employed during the geometry optimization calculations.<sup>9, 10</sup> An energy cut off value of 600 eV has been chosen throughout the calculations. The energy

convergence criteria of  $10^{-6}$  eV have been considered during self-consistent iteration. Brillouin zone has been sampled by  $\Gamma$ -centered k-point mesh of  $5 \times 5 \times 5$  under Monkhorst and Pack scheme.<sup>11</sup> All the model structures have been fully optimized by relaxation of cell parameter, volume and ionic positions. For electronic structure calculations, we have chosen hybrid density functional of the type PBE0,<sup>12</sup> which has been shown to reproduce the experimental band gap nicely.<sup>13</sup> The exchange-correlation energy within the framework of PBE0 ( $E_{XC}^{PBE0}$ ) is expressed as,

$$E_{XC}^{PBE0} = \frac{1}{4}E_X + \frac{3}{4}E_X^{PBE} + E_C^{PBE} \quad (5)$$

The crystal structure figures have been generated using VESTA graphical software.<sup>14</sup>

#### ***S4.2 Defect Formation Energy***

The defect formation energies for the Pr-doped  $Zn_2GeO_4$  in the presence of different defects have been computed using the relationship below.<sup>15, 16</sup>

$$E_{formation} = E_{doped} - E_{perfect} + q \sum n_x \mu_x \quad (6)$$

where,  $E_{doped}$  and  $E_{perfect}$  represent the energy of  $Zn_2GeO_4$  in presence and absence of the dopant element, calculated with same cell size,  $\mu_x$  indicates the chemical potential of the element X and  $n_x$  is the number of elements added ( $q = -1$ ) or replaced ( $q = +1$ ) during the formation of the defect system. The calculated defect formation energies are provided in **Table 1 (main file)**, which indicates that, substitutional doping of Pr into Zn lattice site is energetically more favourable over the interstitial doping. The calculated formation energies for the oxygen vacancy and zinc vacancy defect in the Pr-doped  $Zn_2GeO_4$  are found to be positive, indicating their formation is energetically less favourable.

[**Note:** For modeling Pr interstitial defect, two positions for insertion of Pr atom have been considered. The Pr interstitial atom has been placed both at the center of the Zn ring position ( $Pr_i^1$ ) and Zn-Ge ring position ( $Pr_i^2$ ).]

#### ***S4.3 Role of different defects on the electronic structure of $Zn_2GeO_4$ :***

To investigate the role of different defects on the electronic structure of  $Zn_2GeO_4$  we have analyzed the DOS in the presence of different defects. We will start this discussion with the case of Pr doping into Zn lattice site, which is found to be the most favorable according to the

defect formation energy calculations. As can be seen from **Figure 2 (main file)** that the doping of Pr at the Zn lattice site introduces partially occupied impurity states close to the VBM (0.56 eV above). Analysis of partial density of states (PDOS) reveals that the impurity states are mainly contributed by Pr (f) states. There are no significant changes in the nature of the VBM and CBM. However, the Fermi level appears close to the CBM due to excess electron. The band gap is now reduced to 3.69 eV due to the impurity states. In the presence of oxygen vacancy, the impurity states look little broader (0.32 eV vs 0.10 eV in the absence of vacancy), resulting into the reduction in the band gap to 3.56 eV (**Fig. 2c**). The impurity states in this case are contributed by both Pr (f) (major) and O (p) (minor) states. In the presence of zinc vacancy, additional impurity states (O (p)) appeared at 1.20 eV above the impurity states (Pr (f) and O (p)) adjacent to the VBM, resulting into reduction in the band gap to 2.53 eV (**Fig. 2d**). Now, we proceed to investigate the effect of Zn interstitial defect on the electronic structure of  $\text{Pr}_{\text{Zn}}\text{-Zn}_2\text{GeO}_4$ . For modeling Zn interstitial defect, two different positions for Zn atom insertion have been considered. In one case, the Zn interstitial atom has been placed at the center of the Zn ring position ( $\text{Zn}_i^1\text{-Pr}_{\text{Zn}}\text{-Zn}_2\text{GeO}_4$ ) and in the second case it has been placed at the center of Zn-Ge ring position ( $\text{Zn}_i^2\text{-Pr}_{\text{Zn}}\text{-Zn}_2\text{GeO}_4$ ). **Fig. 2e, f** shows the DOS for the defects,  $\text{Zn}_i^1\text{-Pr}_{\text{Zn}}\text{-Zn}_2\text{GeO}_4$  and  $\text{Zn}_i^2\text{-Pr}_{\text{Zn}}\text{-Zn}_2\text{GeO}_4$ , respectively. In both the cases, additional midgap states introduced along with the impurity states adjacent to the VBM. It can be noted that the impurity states close to the VBM are contributed by Pr (f) states, while other states in the gap regions are hybridized states of host elements. This is beneficial for favorable electronic transition. The effective band gap is found to be significantly reduced due to the presence of impurity states in the forbidden region. As for example, the smallest energy differences between the impurity states are found to be 1.35, 1.64, 0.86, and 1.31 eV for the  $\text{Zn}_i^1\text{-Pr}_{\text{Zn}}\text{-Zn}_2\text{GeO}_4$  system. While the values are 1.69, 1.13, and 0.59 eV for the  $\text{Zn}_i^2\text{-Pr}_{\text{Zn}}\text{-Zn}_2\text{GeO}_4$  system. This will enhance the optical behavior for  $\text{Zn}_2\text{GeO}_4$  system. **Fig. S11(a, b)** show the DOS plot for the  $\text{Pr}_i^1\text{-Zn}_2\text{GeO}_4$ , and  $\text{Pr}_i^2\text{-Zn}_2\text{GeO}_4$ , respectively. Interestingly, Pr (f) impurity states appear in the mid gap region in these cases. This is in contrast to the Pr doping at the Zn lattice site, where Pr (f) impurity states are found to be seen adjacent to the VBM. In these cases, also the effective band gap is found to be reduced significantly. The smallest energy difference between different states were found to be 2.46, 0.92, 1.64, 0.85 eV for the  $\text{Pr}_i^1\text{-Zn}_2\text{GeO}_4$  system, and 1.75, 1.59, 1.48, and 0.89 eV for  $\text{Pr}_i^2\text{-Zn}_2\text{GeO}_4$  system.

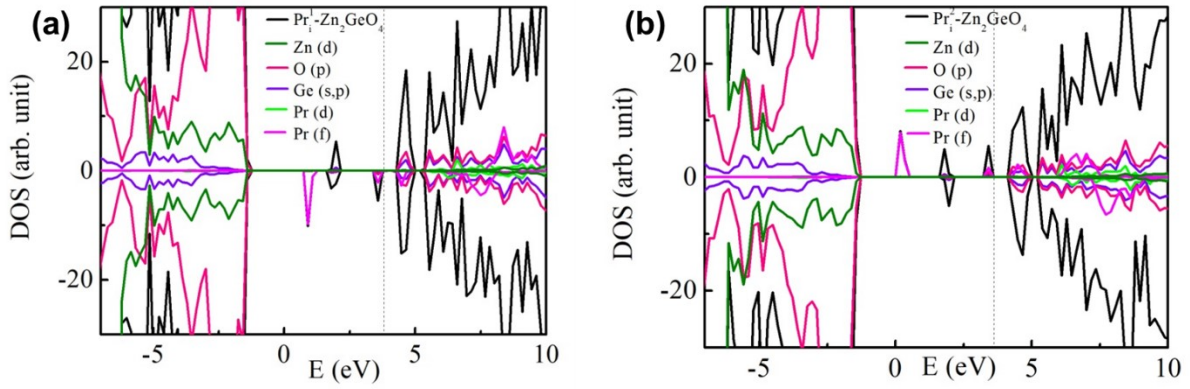


Figure S11: Density of states for  $\text{Zn}_2\text{GeO}_4$  in the presence of Pr at the (a) interstitial site in the Zn ring position ( $\text{Pr}_i^1\text{-Zn}_2\text{GeO}_4$ ), (b) interstitial site in the Zn-Ge ring position ( $\text{Pr}_i^2\text{-Zn}_2\text{GeO}_4$ ). Vertical dashed line indicates the Fermi level.

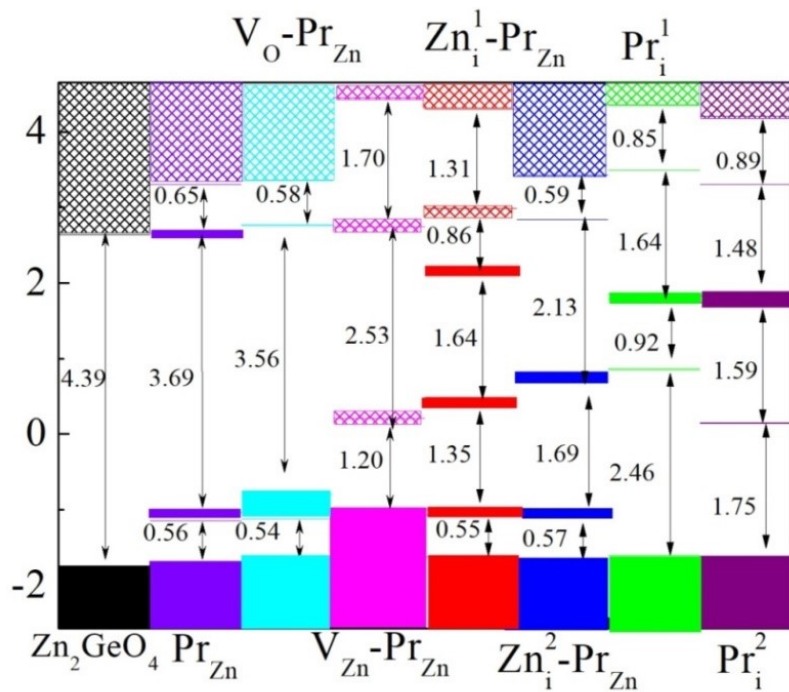


Figure S12: Band edge diagram representing different defect states for Pr substituted at Zn sites.

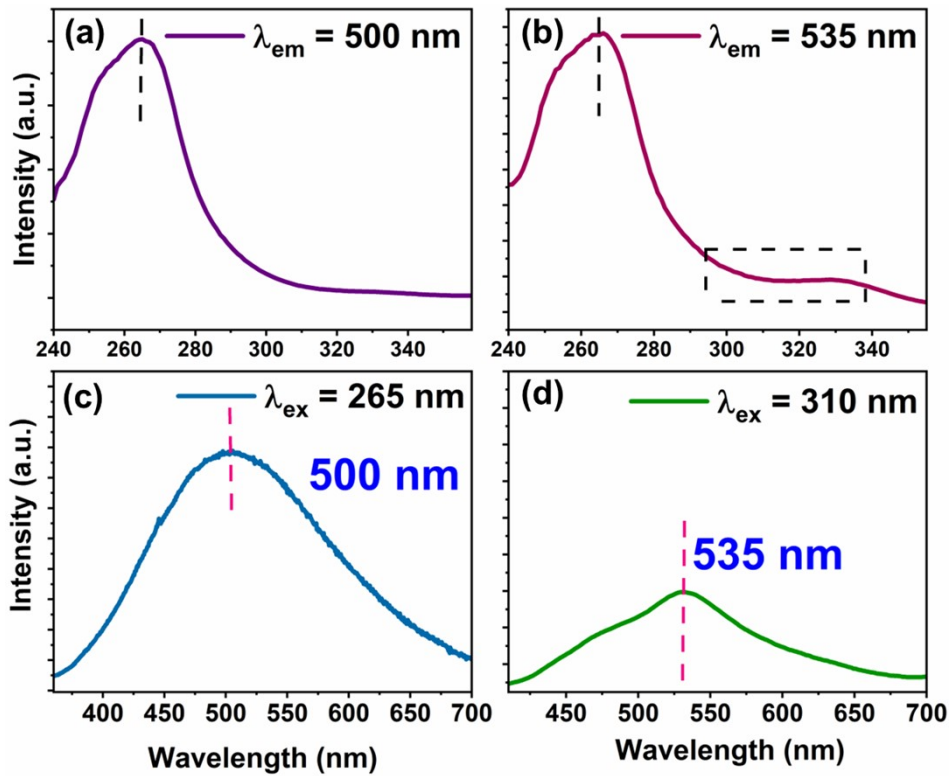


Figure S13: PLE of undoped  $\text{Zn}_2\text{GeO}_4$  monitored at (a) 500 and (b) 535 nm emissions, and PL spectra at (c) 265 nm and (d) 310 nm excitations.

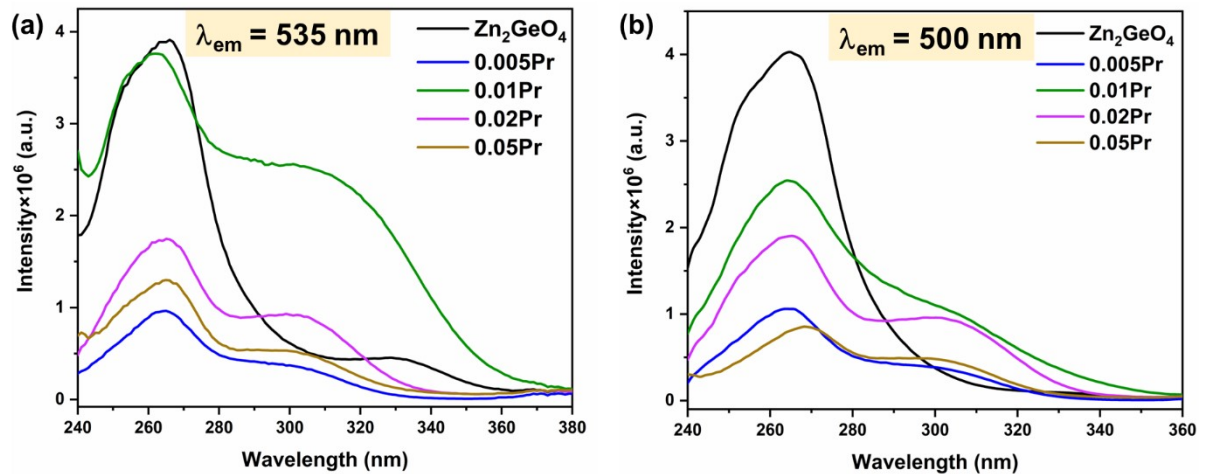


Figure S14: PLE of undoped and  $\text{Pr}^{3+}$  doped  $\text{Zn}_2\text{GeO}_4$  samples monitored at (a) 535 and (b) 500 nm emissions.

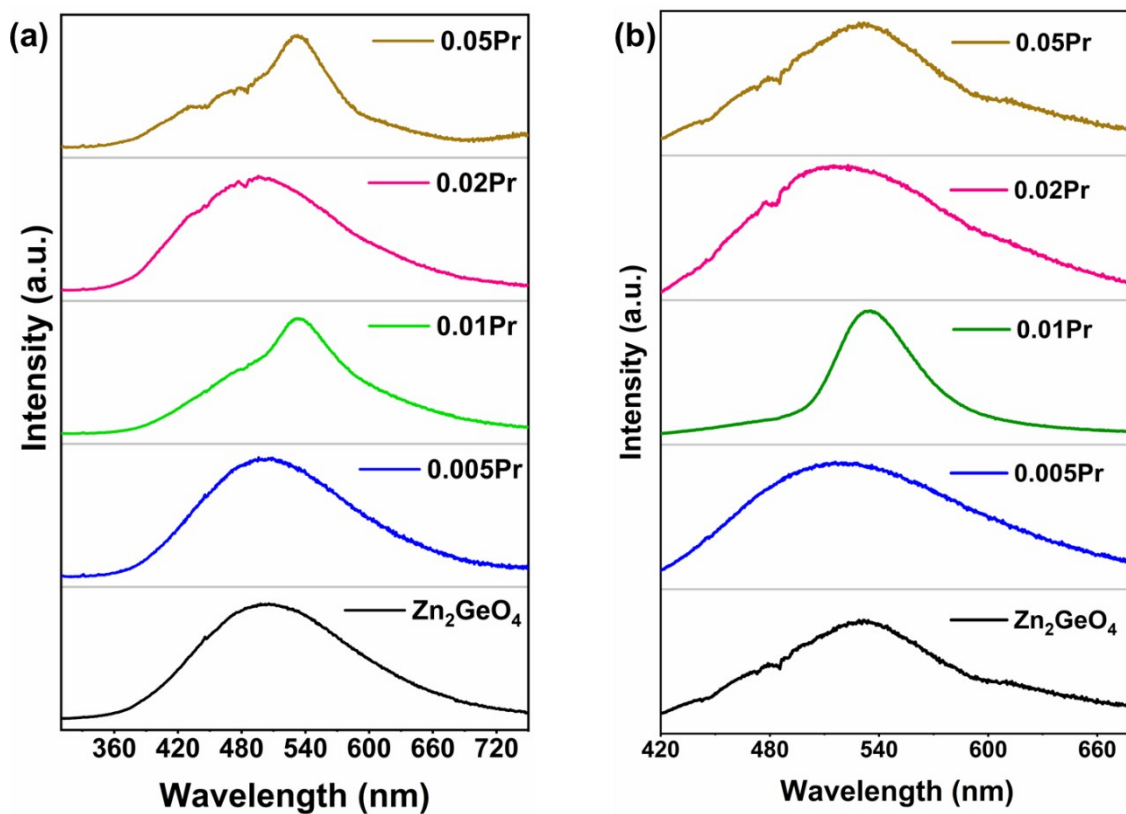


Figure S15: PL emission spectra of undoped and  $\text{Zn}_2\text{GeO}_4:x\text{Pr}^{3+}$  ( $x = 0.005, 0.01, 0.02, 0.05$ ) samples at (a) 265 nm and (b) at 310 nm.

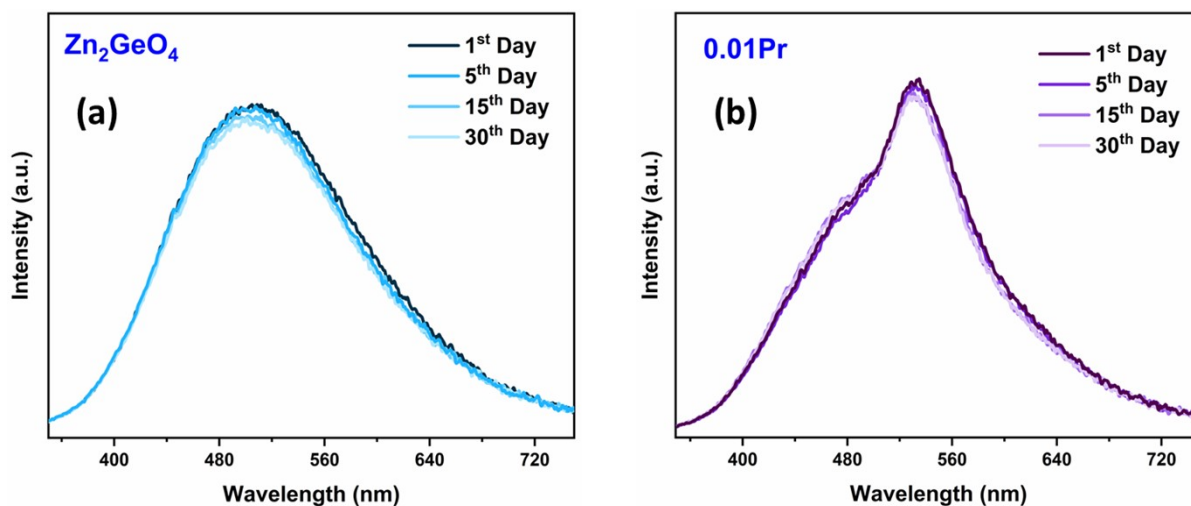
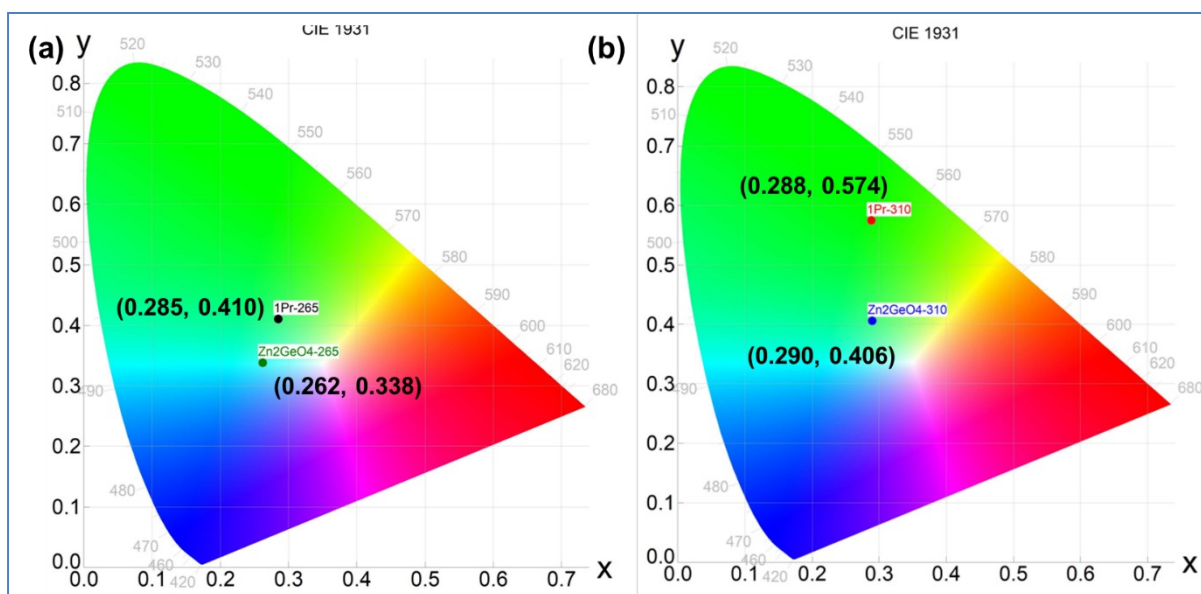
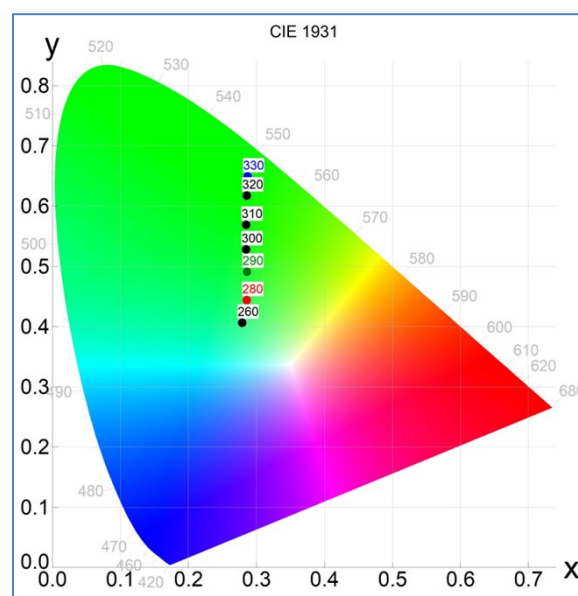


Figure S16: PL Emission spectra of (a)  $\text{Zn}_2\text{GeO}_4$  and (b) 0.01Pr samples recorded on 1<sup>st</sup>, 5<sup>th</sup>, 15<sup>th</sup> and 30<sup>th</sup> day.



**Figure S17: CIE color coordinate diagram for  $\text{Zn}_2\text{GeO}_4$  and 0.01Pr samples at different excitation wavelengths, (a) 265 nm and (b) 310 nm.**



**Figure S18: CIE color coordinate diagram for 0.01Pr sample at different excitation wavelengths in the range of 260 to 330 nm.**

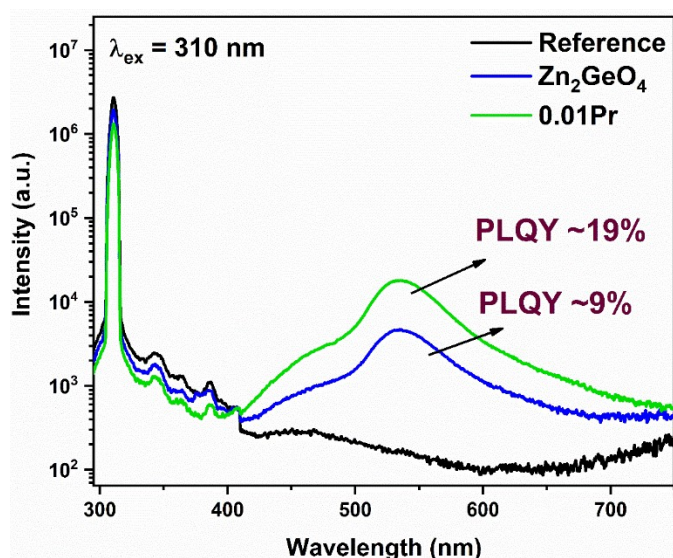


Figure S19: QY spectra of 0.01Pr sample excited at 310 nm.

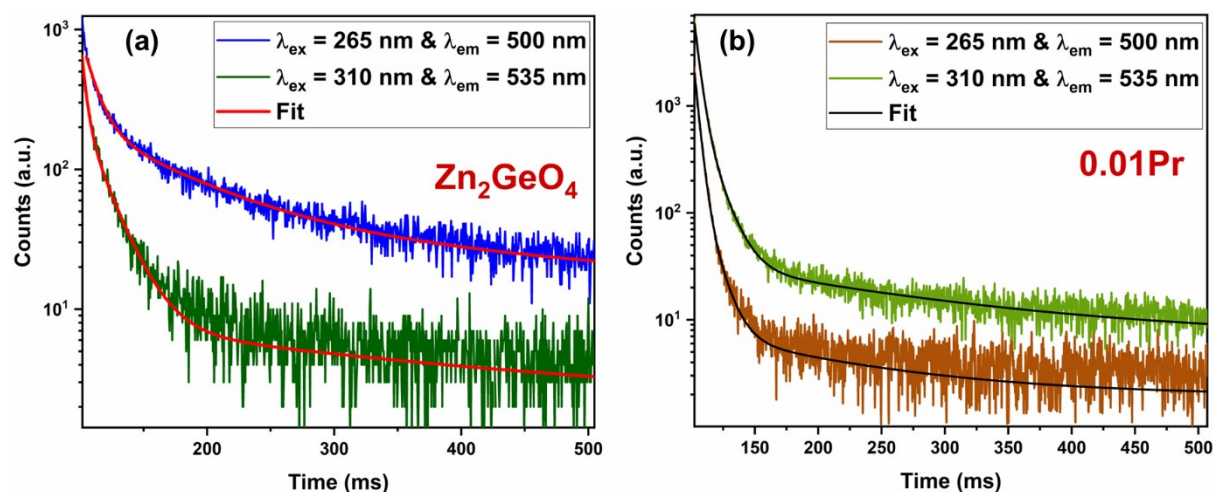


Figure S20: Decay curve of (a)  $\text{Zn}_2\text{GeO}_4$  and (b) 0.01Pr samples monitored at different excitation and emission wavelengths.

Table S4: Luminescence decay lifetimes of  $\text{Zn}_2\text{GeO}_4$  and 0.01Pr samples.

Sample	$\lambda_{\text{ex}}$ (nm)	$\lambda_{\text{em}}$ (nm)	$\tau_1$ (ms)	$I_1\%$	$\tau_2$ (ms)	$I_2\%$	$\tau_3$ (ms)	$I_3\%$	$\tau_{\text{av}}$ (ms)
$\text{Zn}_2\text{GeO}_4$	265	500	3.95	13.1	28.96	33	202.84	53.9	77.01
<b>0.01Pr</b>	265	500	3.32	69.7	9.81	23.1	116.79	7.2	31.56
$\text{Zn}_2\text{GeO}_4$	310	535	3.49	28.3	17.86	52	266.83	19.7	149.03
<b>0.01Pr</b>	310	535	3.79	54.9	11.56	32.5	164.44	12.6	59.25

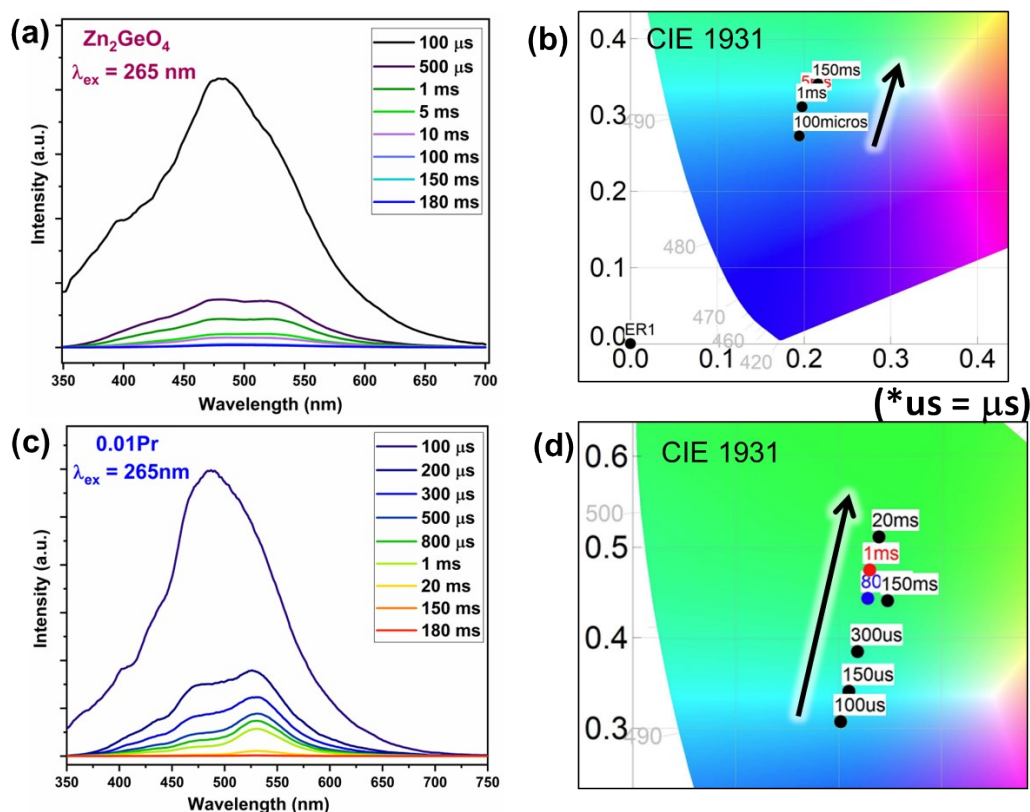


Figure S21: Time-resolved emissions spectra (TRES) at 265 nm excitation at different delay times and CIE color coordinate diagram of (a, b)  $\text{Zn}_2\text{GeO}_4$  and (c, d) 0.01Pr samples, respectively.

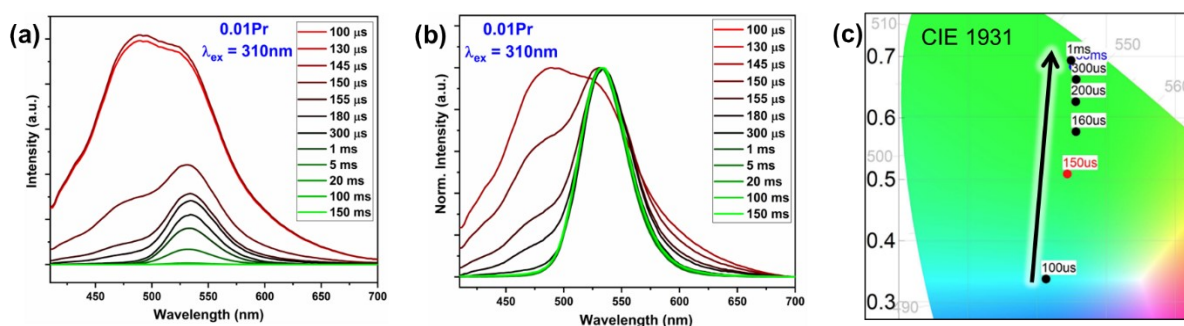


Figure S22: (a) Time-resolved emission spectra (TRES), (b) Normalized TRES of 0.01Pr phosphor at 310 nm excitation at different delay times and (c) CIE color coordinate diagram, respectively.

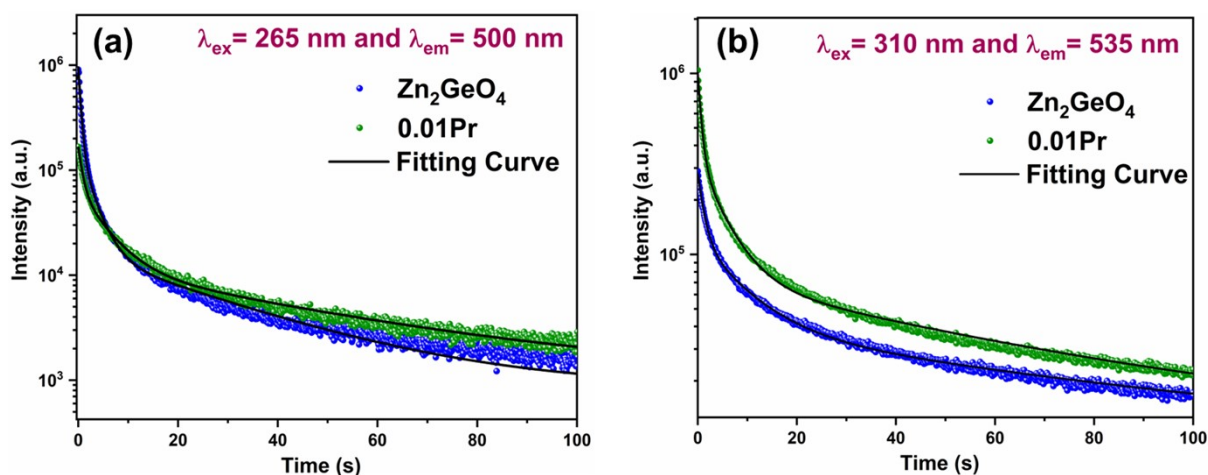


Figure S23: PersL decay curves of  $\text{Zn}_2\text{GeO}_4$  and 0.01Pr phosphors irradiated at (a) 265 nm and (b) 310 nm for 100 s (the black lines are the fitting of decay with three exponential decay function).

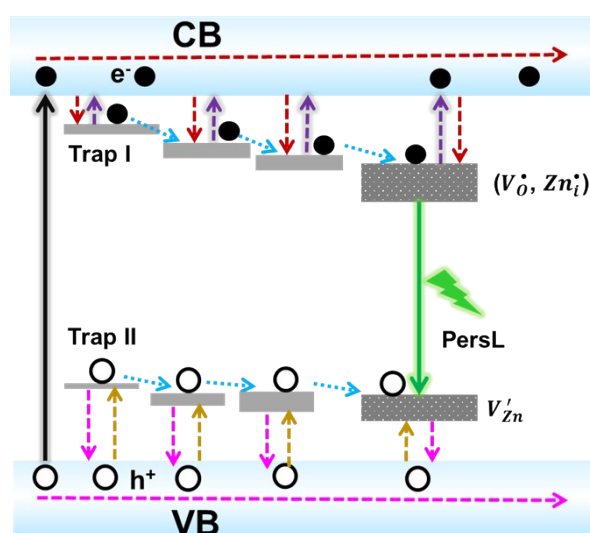


Figure S24: Schematic illustrating the PersL mechanism by electron tunnelling (blue dashed arrows) between trap states. Trapping processes are represented by red and pink dashed arrows for CB and VB, respectively. De-trapping processes are represented by violet and yellow arrows for CB and VB, respectively.

Table S5: Afterglow decay lifetimes of  $\text{Zn}_2\text{GeO}_4$  and 0.01Pr samples.

Sample	$\lambda_{\text{ex}}$ (nm)	$\lambda_{\text{em}}$ (nm)	$\tau_1$ (ms)	$\tau_2$ (s)	$\tau_3$ (s)
$\text{Zn}_2\text{GeO}_4$	265	500	472	2.57	25.29
0.01Pr	265	500	839	5.06	41.59
$\text{Zn}_2\text{GeO}_4$	310	535	1270	9.01	82.68

<b>0.01Pr</b>	310	535	692	5.14	68.40
---------------	-----	-----	-----	------	-------

**Table S6: Comparison Table of some of the recent x-ray persistent phosphors with ZnGe<sub>2</sub>O<sub>4</sub> and 0.01 Pr.**

<b>Phosphor</b>	<b>X-ray Persistent</b>	<b>Remarks</b>	<b>Ref.</b>
Cs <sub>2</sub> NaYF <sub>6</sub> :Pr <sup>3+</sup>	UVC emission lasted for 2h with the strongest output at 1% doping	Fluoride hosts has issue related to its toxic and corrosive nature	17
Sr <sub>2</sub> P <sub>2</sub> O <sub>7</sub> :Gd <sup>3+</sup>	UVB persistent luminescence for more than 24 h	UVB emission has limited commercial viability for solid state lighting. No report of tunability of LED applications	18
Sr <sub>2</sub> MgSi <sub>2</sub> O <sub>7</sub> :Eu <sup>2+</sup> , Dy <sup>3+</sup>	Blue persistent luminescence for around 10 min only.	Low persistent duration, no detailed mechanism and high cost owing to involvement of two rare earth ions	19
ZnGa <sub>1.75</sub> Al <sub>0.25</sub> O <sub>4</sub> :Cr <sup>3+</sup>	Red persistent luminescence for only 100 s.	Very low persistent durations, no detailed study on mechanism and commercial viabilities	20
MgF <sub>2</sub> :Mn <sup>2+</sup>	Green persistent luminescence for only 30 min.	Involvement of fluoride based hosts and requires charging time of 10 min.	21
Tb <sup>3+</sup> -doped fluoride elpasolite	UVB persistent luminescence for more than 50 h	Involvement of fluoride host, long charging time, emission of non-visible light, etc.	22
CsCdCl <sub>3</sub> , Mn <sup>2+</sup> , Zr <sup>4+</sup>	Persistent light for 12h	But requires additional charging by 980 nm laser.	23
Zn <sub>2</sub> GeO <sub>4</sub> :1%Pr <sup>3+</sup>	Persistent light for more than 18h	Stable host, tunable light on doping, high thermal stability, potential for LED fabrication, etc.	<b>This work</b>

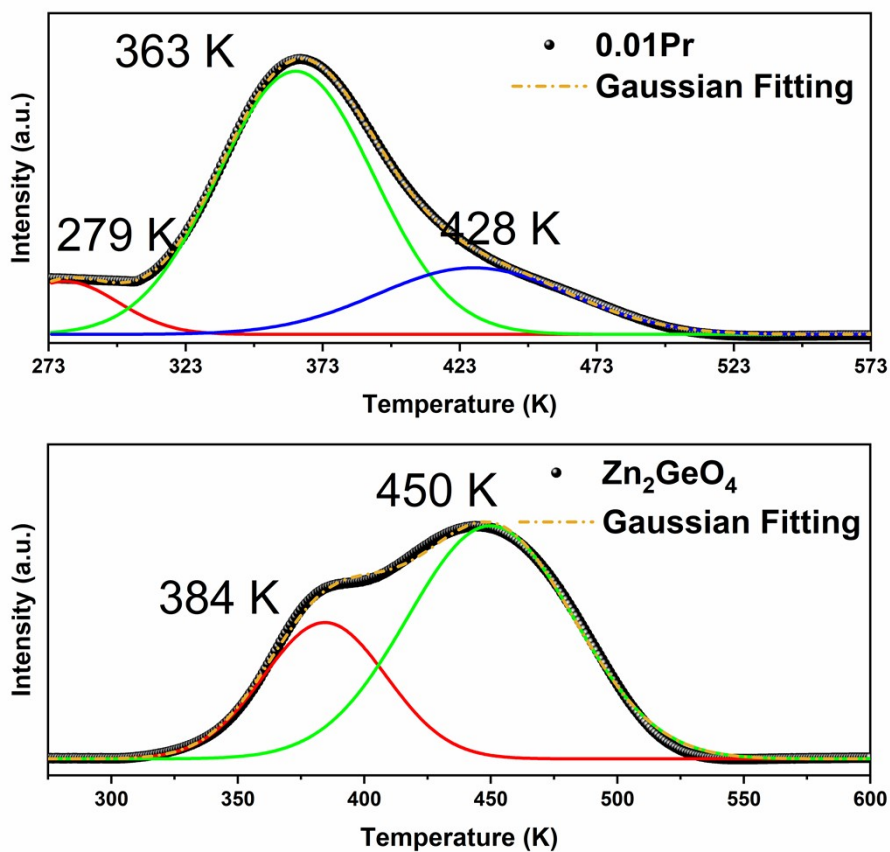


Figure S25: Thermoluminescence (TL) glow curves and Gaussian deconvoluted peaks of undoped and 0.01Pr phosphors.

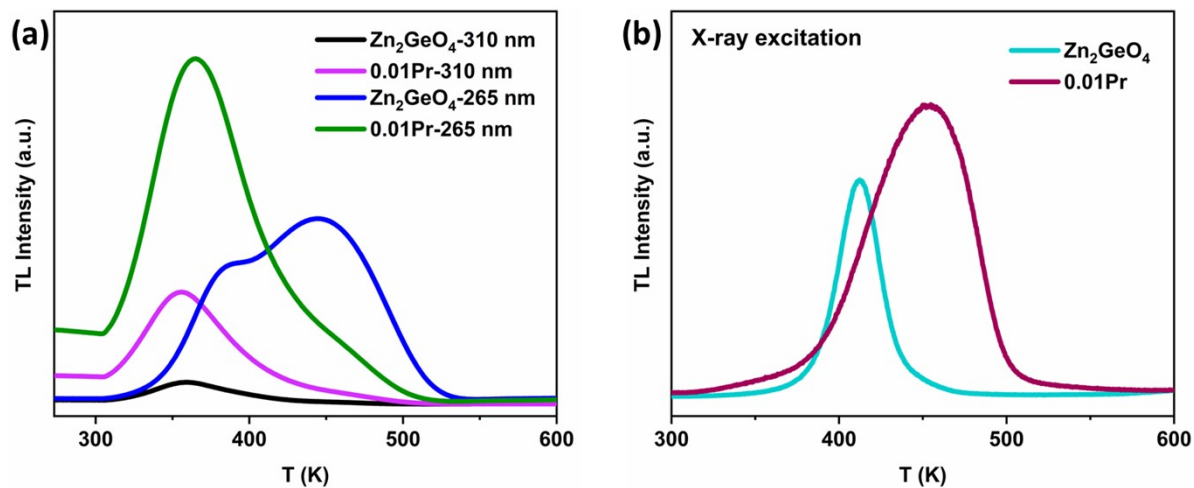


Figure S26: TL glow curves of  $\text{Zn}_2\text{GeO}_4$  and 0.01Pr phosphors for (a) 310 and 365 nm irradiation with xenon lamp, and (b) after X-ray irradiation.

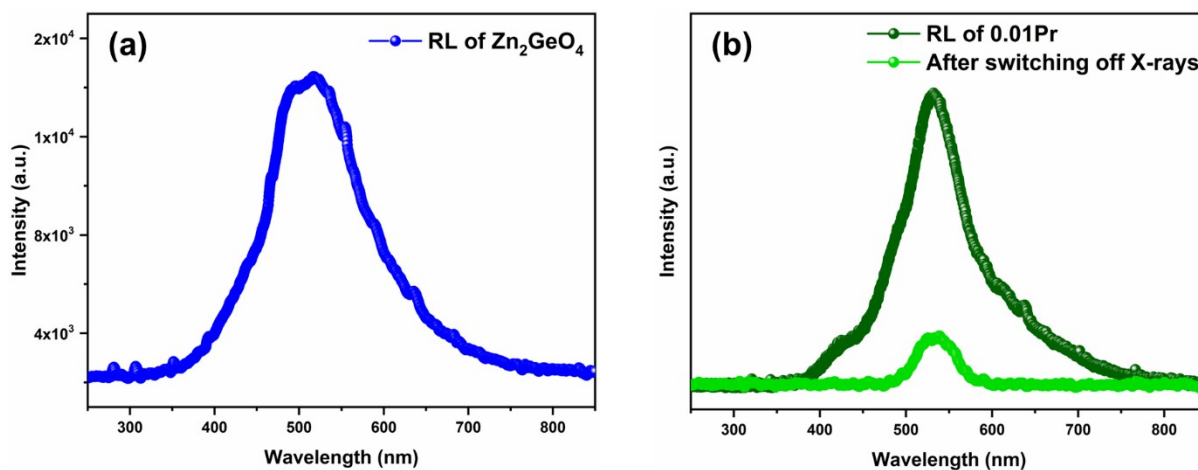


Figure S27: (a) Radioluminescence (RL) spectra of (a) undoped sample, and (b) RL afterglow spectra of 0.01Pr sample.

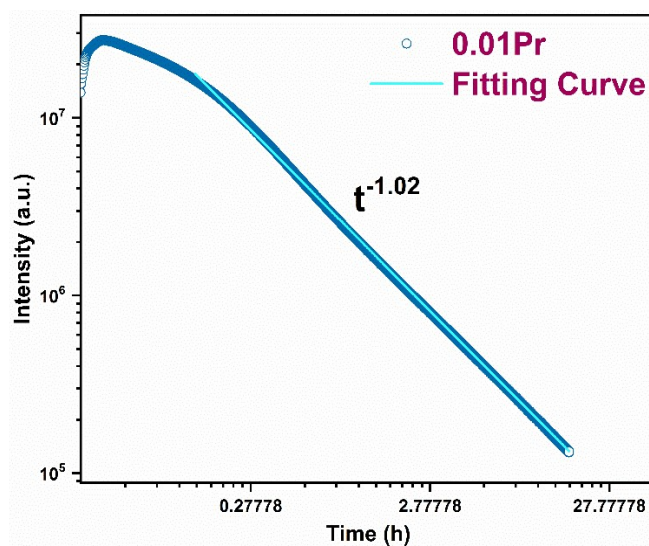


Figure S28: Fitting of X-ray activated PersL intensity as a function of ( $t^{-a}$ ) for 0.01Pr sample.

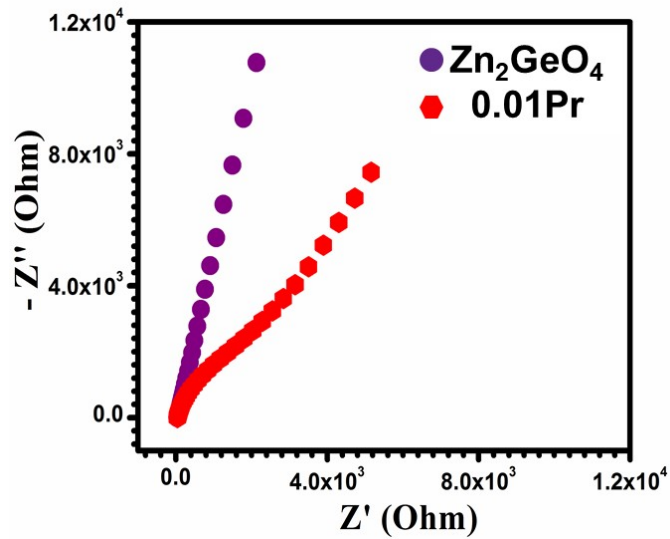


Figure S29: Electrochemical impedance of undoped  $Zn_2GeO_4$  and 0.01Pr samples.

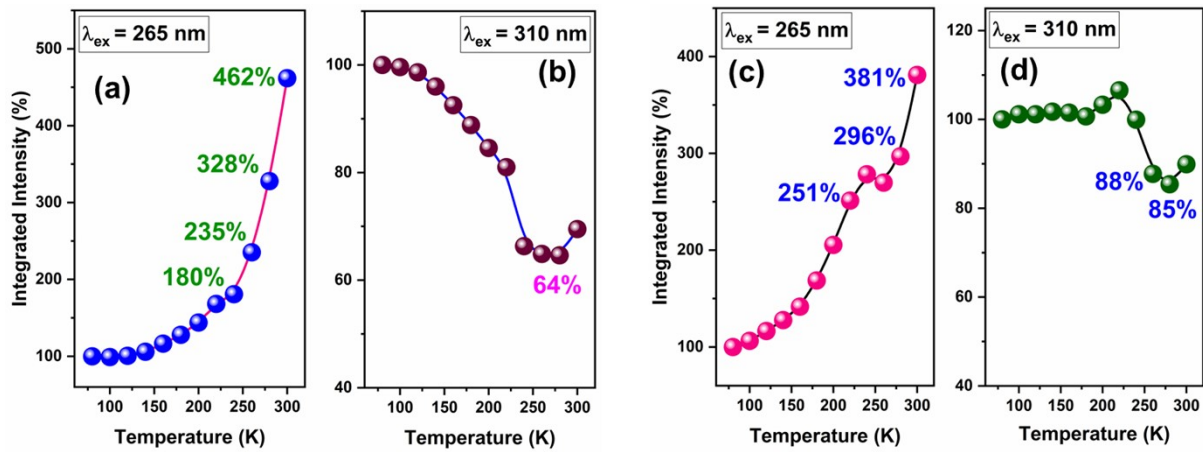


Figure S30: Intensity change as a function of temperature for PL bands of (a, b)  $Zn_2GeO_4$  and (c, d) 0.01Pr at 265 and 310 nm excitation, respectively.

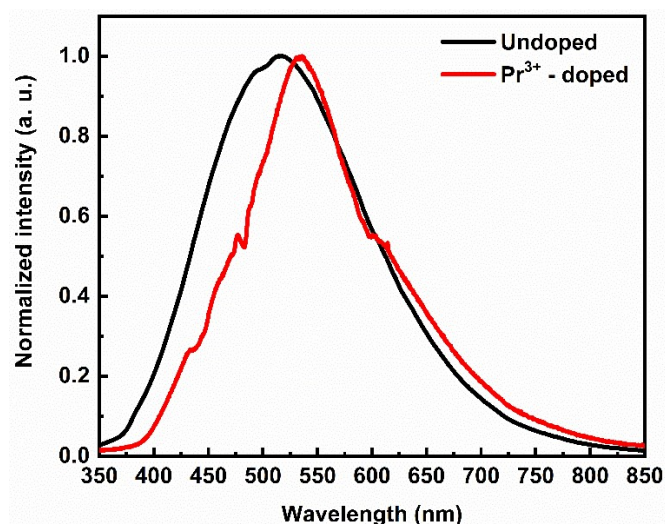


Figure S31: EL spectral comparison for  $\text{Zn}_2\text{GeO}_4$  and 0.01Pr samples.

#### References:

1. Basu, S.; Nayak, C.; Yadav, A.; Agrawal, A.; Poswal, A.; Bhattacharyya, D.; Jha, S.; Sahoo, N. In *A comprehensive facility for EXAFS measurements at the INDUS-2 synchrotron source at RRCAT, Indore, India*, Journal of Physics: Conference Series, 2014; IOP Publishing: 2014; p 012032.
2. Poswal, A.; Agrawal, A.; Yadav, A.; Nayak, C.; Basu, S.; Kane, S.; Garg, C.; Bhattachryya, D.; Jha, S.; Sahoo, N. In *Commissioning and first results of scanning type EXAFS beamline (BL-09) at INDUS-2 synchrotron source*, AIP Conference Proceedings, 2014; American Institute of Physics: 2014; pp 649-651.
3. Bunker, G., *Introduction to XAFS: a practical guide to X-ray absorption fine structure spectroscopy*. Cambridge University Press: 2010.
4. Kelly, S.; Hesterberg, D.; Ravel, B., Analysis of soils and minerals using X-ray absorption spectroscopy. *Methods of soil analysis part 5—mineralogical methods* 2008, 5, 387-463.
5. Koningsberger, D. C.; Prins, R., X-ray absorption: principles, applications, techniques of EXAFS, SEXAFS and XANES. 1987.
6. Ravel, B.; Newville, M., ATHENA, ARTEMIS, HEPHAESTUS: data analysis for X-ray absorption spectroscopy using IFEFFIT. *Journal of synchrotron radiation* 2005, 12, (4), 537-541.
7. Blöchl, P. E., Projector augmented-wave method. *Physical Review B* 1994, 50, (24), 17953.
8. Kresse, G.; Joubert, D., From ultrasoft pseudopotentials to the projector augmented-wave method. *Physical Review B* 1999, 59, (3), 1758.
9. Perdew, J. P.; Burke, K.; Ernzerhof, M., Generalized gradient approximation made simple. *Physical review letters* 1996, 77, (18), 3865.
10. Perdew, J. P.; Chevary, J. A.; Vosko, S. H.; Jackson, K. A.; Pederson, M. R.; Singh, D. J.; Fiolhais, C., Atoms, molecules, solids, and surfaces: Applications of the generalized gradient approximation for exchange and correlation. *Physical Review B* 1992, 46, (11), 6671.
11. Monkhorst, H. J.; Pack, J. D., Special points for Brillouin-zone integrations. *Physical Review B* 1976, 13, (12), 5188.
12. Perdew, J. P.; Ernzerhof, M.; Burke, K., Rationale for mixing exact exchange with density functional approximations. *The Journal of chemical physics* 1996, 105, (22), 9982-9985.

13. Gupta, S. K.; Sudarshan, K.; Modak, B.; Gupta, R., Interstitial Zinc Boosted Light Tunability, Afterglow, and Ultrabright White Emission in Zinc Germanate ( $\text{Zn}_2\text{GeO}_4$ ). *ACS Applied Electronic Materials* 2023, 5, (2), 1286-1294.
14. Momma, K.; Izumi, F., VESTA: a three-dimensional visualization system for electronic and structural analysis. *Journal of Applied Crystallography* 2008, 41, (3), 653-658.
15. Modak, P.; Modak, B., Exploring the role of vacancy defects in the optical properties of  $\text{LiMgPO}_4$ . *Physical Chemistry Chemical Physics* 2020, 22, (28), 16244-16257.
16. Modak, P.; Modak, B., Electronic structure investigation of intrinsic and extrinsic defects in  $\text{LiF}$ . *Computational Materials Science* 2022, 202, 110977.
17. Yang, Y.-M.; Li, Z.-Y.; Zhang, J.-Y.; Lu, Y.; Guo, S.-Q.; Zhao, Q.; Wang, X.; Yong, Z.-J.; Li, H.; Ma, J.-P.; Kuroiwa, Y.; Moriyoshi, C.; Hu, L.-L.; Zhang, L.-Y.; Zheng, L.-R.; Sun, H.-T., X-ray-activated long persistent phosphors featuring strong UVC afterglow emissions. *Light: Science & Applications* 2018, 7, (1), 88.
18. Zhang, Y.; Liang, Y.; Shan, X.; Chen, D.; Miao, S.; Shi, R.; Xie, F.; Wang, W., X-ray-Excited Long-Lasting Narrowband Ultraviolet-B Persistent Luminescence from  $\text{Gd}^{3+}$ -Doped  $\text{Sr}_2\text{P}_2\text{O}_7$  Phosphor. *Inorganic Chemistry* 2022, 61, (50), 20647-20656.
19. Homayoni, H.; Sahi, S.; Ma, L.; Zhang, J.; Mohapatra, J.; Liu, P.; Sotelo, A. P.; Macaluso, R. T.; Davis, T.; Chen, W., X-ray excited luminescence and persistent luminescence of  $\text{Sr}_2\text{MgSi}_2\text{O}_7:\text{Eu}^{2+}, \text{Dy}^{3+}$  and their associations with synthesis conditions. *Journal of Luminescence* 2018, 198, 132-137.
20. Gupta, S. K.; Sudarshan, K.; Modak, P.; Chandrashekhar, D.; Tyagi, M.; Modak, B.; Mohapatra, M., Design of need-based phosphors and scintillators by compositional modulation in the  $\text{ZnGa}_{2-x}\text{Al}_x\text{O}_4:\text{Cr}^{3+}$  spinel: pure compound versus solid solutions. *Physical Chemistry Chemical Physics* 2022, 24, (38), 23790-23801.
21. Ma, M.; Li, L.; Cai, C.; Han, Y.; Yang, Y., X-ray excited  $(\text{Mg,Ca})\text{F}_2:\text{Mn}^{2+}$  for persistent luminescence modulation. *Journal of Luminescence* 2022, 252, 119376.
22. Li, Z.; Li, H.; Sun, H.-T., X-ray-activated UVA long persistent luminescence from defective fluoride elpasolites. *Journal of Rare Earths* 2020, 38, (2), 124-129.
23. Zhou, X.; Han, K.; Wang, Y.; Jin, J.; Jiang, S.; Zhang, Q.; Xia, Z., Energy-Trapping Management in X-Ray Storage Phosphors for Flexible 3D Imaging. *Advanced Materials* 2023, 35, (16), 2212022.